Modeling carrier mobility in graphene as a sensitive probe of molecular magnets

Andrew Brooks [1,2] Tao Jiang,[3,2] Shuanglong Liu,[1,2] Duy Le [3,2] Talat S. Rahman,[3,2] Hai-Ping Cheng,[1,2]
and Xiao-Guang Zhang [1,2,*]

[1]*Department of Physics and Quantum Theory Project, University of Florida, Gainesville, Florida 32611, USA*
[2]*Center for Molecular Magnetic Quantum Materials, University of Florida, Gainesville, Florida 32611, USA*
[3]*Department of Physics, University of Central Florida, Orlando, Florida 32816, USA*

Carrier mobility in graphene on a GaAs substrate and its change due to the adsorption of molecular magnets, Mn_{12} and $[Mn_3]_2$, on the surface of graphene, is calculated from first principles. Phonon limited mobility is also calculated for comparison. For Mn_{12} adsorption on graphene, the mobility is compared for different organic ligands of Mn_{12} (-H, -CH_3, and -$CHCl_2$), while for $[Mn_3]_2$ dimers, the mobility is calculated for different linkers that yield the ferromagnetic and anti-ferromagnetic configurations of $[Mn_3]_2$, as well as for different orientations of the molecule. Significant changes in carrier mobility due to the adsorption of the molecules and due to differences in linkers suggest mobility measurement as a possible sensitive probe of magnetic molecules.

I. INTRODUCTION

Graphene has long been proposed as a sensitive probe of molecules [1–5] because of its gate tunable carrier density and high carrier mobility [1]. A recent experiment demonstrated that electron transport measurements of graphene can be used to probe the electronic and magnetic properties of molecules deposited on a graphene substrate [6]. One of the physical quantities measured that showed strong sensitivity to the magnetic molecules is the carrier mobility in graphene. This experiment naturally leads to the question whether one can use measurements of mobility in a graphene sheet to detect and determine the electronic structure and magnetic states of molecular magnets.

One such molecule that has been studied in the context is Mn_{12} [$Mn_{12}O_{12}(O_2CR)_{16}(H_2O)_4$] [7], a widely studied single molecule magnet (SMM) owing to its large magnetic anisotropy barrier [8] which makes it ideal for data storage devices [9] and quantum computing applications [10]. In the chemical formula, R is an organic ligand. In this study, we consider the ligands -H, -CH_3, and -$CHCl_2$. The magnetic properties of Mn_{12} have a strong dependence on the ligands [11–15]. Previous density functional theory (DFT) study shows that the interaction of Mn_{12} with a graphene substrate is also sensitive to the type of ligands [7].

Another interesting Mn-based magnetic molecule is $[Mn_3]_2$, which consists of two triangular units of Mn_3 linked covalently by three dioximate ligands (linkers) [16]. The spin alignment of the dimer can be ferromagnetic (FM) or antiferromagnetic (AFM) depending on the linkers [17]. The chemical formula for an example of the AFM $[Mn_3]_2$ dimer is $[Mn_6O_2(O_2CMe)_6 6(ada)_3]^{2+}$ where the ada^{2-} group is the anion of 1,3-adamantanedicarboxylate.

The formula for an example of the FM $[Mn_3]_2$ dimer is $[Mn_6O_2(O_2CMe)_6(dpd)_3]^{2+}$, where the dpd^{2-} group is the anion of 1,3-di(pyridin-2-yl)propane-1,3-dione dioxime.

In this paper, we develop a method for the calculation of carrier mobility in graphene limited by adsorbed molecule without the explicit inclusion of the molecule and calculate the in-plane carrier mobility graphene limited by either phonons or the adsorption of magnetic molecules (Mn_{12} and $[Mn_3]_2$) from the complex band structure obtained using a density-functional theory based method [18,19]. For Mn_{12}, we calculate the carrier mobility with different attached ligands (-H, -CH_3, and -$CHCl_2$). For $[Mn_3]_2$ dimer, the carrier mobility is compared between different linkers that produce AFM and FM ground states of the dimer, as well as for different orientations of the $[Mn_3]_2$ dimers on graphene surface [20].

II. METHOD

The method utilizes a complex energy to model the finite lifetime of the Bloch state, due to scattering by defects, or deviation from crystallinity, as described in Ref. [21]. We calculate the complex band structure (CBS) of two related systems which we call the real medium (system with defects) and the effective medium (system without defect) using QUANTUM ESPRESSO [22,23]. Our goal is to add a constant complex energy Σ to the effective medium to match the scattering effects in the real medium, which according to the method, is achieved when the complex wave vector from both media are brought into agreement (Fig. 1). The complex energy Σ plays the role of a self-energy that would arise from configurational average over disorder. We will show later that Σ is distinct from self-energy due to interaction with external electrodes or molecules. The imaginary part of Σ is related to the mean scattering time τ,

$$\text{Im}\Sigma = \hbar/2\tau. \tag{1}$$
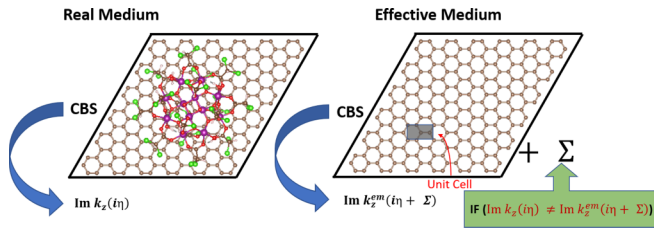
*xgz@ufl.edu

245423-1

FIG. 1. A summary of how Σ is deduced from the complex band as illustrated by a SMM on the surface of graphene. A single CBS calculation of the real medium is needed to produce a complex wave vector at a complex energy $\epsilon + i\eta$ where the imaginary part η provides screening. Iterative CBS calculation of the effective medium (pristine graphene) at energy $\epsilon + \Sigma + i\eta$ is performed while tuning the self-energy Σ until the complex wave vector agrees with that obtained in the real medium.

We then use the linear Boltzmann theory to calculate the in-plane carrier mobility

$$\mu = -\frac{2e}{n_c} \sum_j \int d^2\mathbf{k} \frac{\tau_j(\mathbf{k})}{(2\pi)^2} v_j^2(\mathbf{k}) \frac{\partial f(\epsilon_{\mathbf{k}j})}{\partial \epsilon_{\mathbf{k}j}}, \qquad (2)$$

where n_c is the free electron carrier density, v is the electron velocity in the transport direction, f is Fermi-Dirac distribution function, and the sum is taken over the valley degeneracy (two in the case of graphene, Fig. 2). The carrier density is given by

$$n_c = \frac{2}{(2\pi)^2} \sum_j \int d^2\mathbf{k} f(\epsilon) = \frac{2}{\pi c^2} \int d\epsilon \, \epsilon f(\epsilon), \quad (3)$$

where we employ graphene's linear dispersion relation for carriers near the Dirac point, $\epsilon = c|k|$ and perform a change of variables from the magnitude of the wave vector k to the electron energy. We assume that the mean scattering time is only weakly dependent on the electron's energy so that it can be replaced by a constant τ_0 which we take to be the mean scattering time at the most probable electron energy. Utilizing this assumption, we can rewrite the mobility as

$$\mu = \frac{ec^2\tau_0}{2\hbar^2} \frac{\int_0^\infty d\epsilon \, f(\epsilon)}{\int_0^\infty d\epsilon \, \epsilon f(\epsilon)}. \qquad (4)$$
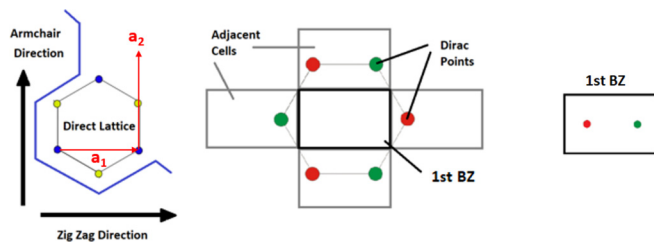

FIG. 2. (Left) Lattice vectors of a $1 \times \sqrt{3}$ graphene supercell for the complex band calculation. The $\mathbf{a_1}$ and $\mathbf{a_2}$ lattice vectors of the supercell lie along the armchair and zigzag directions, respectively. (Middle) Positions of the Dirac points for a primitive graphene cell in the reciprocal space of the $1 \times \sqrt{3}$ graphene supercell. The boundary of the first Brillouin zone (BZ) is illustrated by bold lines. (Right) The Dirac points are folded into the first Brillouin zone at $(\pm\frac{1}{3}\frac{2\pi}{a_1}, 0)$.

Since the transmission probability of the electron through a section of the medium depends uniquely on its imaginary part of the complex wave vector [21], the complex self-energy Σ applied to the effective medium is tuned until the imaginary part of the electron's wave vector is the same in both media.

In addition to Σ needed to produce the same scattering effects in the effective medium as the real medium, we also need to add a small imaginary energy, $i\eta$ to minimize the interference between scatterers of adjacent supercells. The size of this imaginary energy, herein referred to as the screening parameter, is estimated using

$$\eta = \frac{2\hbar v_F}{L}, \qquad (5)$$

where v_F is the Fermi velocity and L is the length of the supercell in the direction of transport. It will induce some small error on the complex band structure by introducing new scattering effects. Thus we also add this energy to the effective medium to cancel out the errors when comparing the complex band structures.

Another error that can be introduced by adding $i\eta$ is the distortion of the real bands, in addition to its effect of smearing. This can lead to the calculated wave vector to deviate from the wave vector without η. Because such deviation is linear in η, the consequence of this error is that the extracted Σ is linear with η, rather than independent of it. To correct this error without having to find the distorted real band structure, one can adjust (k_x, k_y) and find the transverse wave vector that yields the smallest Im k_z for a fixed η (Fig. 3). This ensures that the calculated Σ is independent of η. When the transport direction is in the armchair direction we move k_x by $0.005 \, (2\pi/a)$ towards the Γ point, where a is the length of the lattice constant of graphene, for the size of the supercell and $i\eta$ we use.

The carrier density and the mobility depend on the placement of the Fermi level. Puddling of the free carriers on the surface of graphene is known to occur for carrier densities as high as 10^{12} cm^{-2} and higher due to charge impurities that may be present in the graphene environment [8], and contributes to the local variation of the Fermi level away from the charge neutral point. We consider the effect of the puddling of carriers on graphene by assuming that the fluctuation of the local Fermi level is distributed according to a Gaussian distribution [8]. We have found from our calculations that the self-energy obtained from the complex band calculation is mostly constant at energies near the Dirac point. The average carrier mobility is obtained by an ensemble average over different Fermi levels.

A. Molecular pseudopotential

The real medium consists of the relaxed graphene/molecule structure. For a large supercell, calculating the complex band structure of this structure can be prohibitively expensive, as is the case when we place a large molecule on the surface of graphene. However, as the molecules are physisorbed and at about 2.5 Å away from the surface of graphene, we do not expect the electronic states in the molecule to significantly impact the orbital make-up of the Bloch states within graphene except to establish an
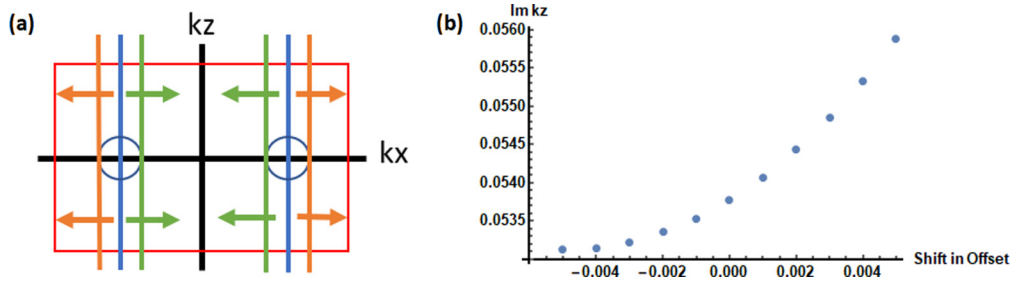
FIG. 3. Dependence of Im k_z with a shift in the offset k_x away from the Dirac point when the z axis is aligned with the armchair direction. (a) The reciprocal cell of a single orthogonal unit cell. The circles represent the undistorted energy surface centered around the Dirac points. The k_x offset (in units of $\frac{2\pi}{a}$) can be set on the Dirac point (blue lines) or be shifted away from the Dirac point either towards the Γ point (green) or away (orange). (b) The dependence of the Im k_z (in units of $\frac{2\pi}{a\sqrt{3}}$) on the offset shifting away from the Dirac point. Negative (positive) shift represent shifts towards (away from) the Γ point.

electrostatic potential external to the graphene, as we shall demonstrate in this section. Therefore, in the complex band calculation, we replace the actual molecule by an effective electrostatic potential as we describe below.

The general form of an atomic pseudopotential contains both a local potential and a nonlocal potential. We perform the complex band structure calculation by removing the molecule all together and modifying the local potential of the displaced graphene with the addition of the following difference:

$$\delta V = V_{\text{Mol.+Gr}} - V_{\text{Gr}}, \tag{6}$$

where $V_{\text{Mol.+Gr}}$ and V_{Gr} are the total local potentials of the graphene with and without the molecule on the surface obtained from the self-consistent calculation, respectively, and we disregard the short-ranged, nonlocal parts of the pseudopotentials that are associated with atoms of the molecule. In this way, the modified local potential of the perturbed graphene accounts approximately for the total effect of the adsorbed molecule without explicitly including the molecule in the complex band structure calculations.

As mentioned above, computing the complex band structure of the graphene-SMM structure is prohibitively expensive, computationally. Thus we demonstrate here that the molecule can be replaced with such a potential by calculating the in-plane carrier mobility for graphene in the presence of a water molecule above graphene surface. For this system, we can calculate the complex band structure directly, and we can compare the complex band structure of the system without the molecule but including the δV potential, and with graphene only.

The self-energy Σ extracted from the complex band calculation for each system is shown in Table I. In all of these calculations, the transport direction is in the armchair direction (Fig. 2). The graphene calculation with water molecule is fully relaxed, thus the scattering effects are introduced via the displaced graphene and the presence of water on the surface. The graphene only calculation is done using only the graphene from the fully relaxed Gr + H$_2$O system. The scattering from only the displaced graphene is significantly less than that calculated when both the displaced graphene and the water molecule are included, which can be seen from Table I manifested by a smaller self-energy. The similarity of the self-energy calculated with two approaches, i.e., Gr + δV and Gr + H$_2$O indicates that the majority of the scattering effect in

the Gr+H$_2$O system is due to the external potential induced on the graphene by the water molecule, while the displacement of the graphene from it's ideal coordinates is only a minor contribution to the scattering. The δV approach to calculating the self-energy becomes computationally advantageous when the molecules on the surface of graphene contains a significant number of atoms, as is the case with Mn$_{12}$ and [Mn$_3$]$_2$.

We emphasize that the self energy calculated here is the self-energy due to the disorder introduced by having some concentration of molecules on the surface of the graphene. A small coupling between the electronic states of the molecule and graphene will only contribute a small effect on electronic states associated with the graphene. The real band structure is shown in Fig. 4 near the Dirac point for all three systems (Gr-Only, Gr + δV, Gr+H$_2$O), which is virtually the same for all three systems and implies that the coupling between the electronic states of the molecule and the graphene is extremely weak. Thus contribution from such coupling to the graphene self-energy is negligible. On the other hand, the potential of the molecule contributes to the disorder that exists within the graphene and thus contributes to the complex self energy Σ. This latter effect is adequately included in our model by δV.

In addition, by removing the SMM, the length of the supercell perpendicular to the graphene layer can be reduced as it is no longer necessary given the SMM has been removed. In reducing the size of the supercell, we make sure that the δV potential should tend to zero at the boundary above and below the graphene layer. As only the potential near the graphene layer should have an impact on the graphene Bloch states. We apply a Gaussian envelope to the δV potential with the graphene layer centered in the supercell to gradually reduce

TABLE I. The imaginary part of the self-energy Σ of a graphene sheet due to an adsorbed H$_2$O molecule calculated under three approximations. Gr-Only: with H$_2$O removed but using C coordinates calculated with H$_2$O. Gr + δV: with H$_2$O removed but using δV and C coordinates calculated with H$_2$O. Gr + H$_2$O: Full calculation with H$_2$O.

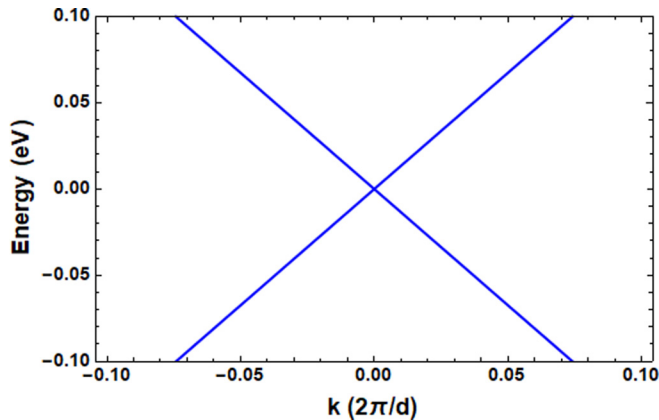| System	Σ (μeV)
Gr-Only	4.31
Gr + δV	28.1
Gr + H$_2$O	25.3

FIG. 4. The band structure of the Gr-Only, Gr + H₂O, and Gr + δV near the Dirac point. The three cases are indistinguishable and appear as the same band structure in the plot. The size of the supercell maps the location of the Dirac point to Γ, and k is in units of $2\pi/d$, where $d = 6(2.46)\sqrt{3}$ Å is the length of the supercell in the transport direction

the potential so that it is negligible at the boundaries across from graphene.

III. COMPUTATIONAL DETAILS

The structural relaxations of Mn_{12} on graphene and $[Mn_3]_2$ dimers on graphene were carried out on the basis of DFT [18,19] as implemented in the Vienna *ab initio* simulation package (VASP) [24,25] and in the QUANTUM ESPRESSO suite [26], respectively. The kinetic energy cutoff was set to 500 eV for plane waves in VASP, 680 eV for the plane-wave expansion of wave functions in QUANTUM ESPRESSO, and 4760 eV for the plane-wave expansion of charge density in QUANTUM ESPRESSO. In all calculations the electron-ion interactions were described by the projector-augmented wave (PAW) pseudopotential method [27,28]. The exchange correlation effects were implemented by the generalized-gradient approximation (GGA) in the form of Perdew-Berke-Enzerhoff (PBE) exchange-correlation functionals [28] together with DFT-D3 correction [29] to account for the van der Waals interaction. The Brillouin zone was sampled with one point at the zone center. The energy and force tolerances were below 1.5×10^{-5} eV and 0.03 eV/Å, respectively. In order to minimize the artificial interaction between periodic images in the out-of-plane direction, a vacuum of 15 Å or more thick is added. For the same purpose, dipole correction [30] was also applied for $[Mn_3]_2$ dimers on graphene.

To calculate the complex band structure, we use the PWCOND [22,23] code within the QUANTUM ESPRESSO suite, locally modified to allow for the calculation of the complex wave vector with respect to a complex energy [31] and to allow for the total local potential to be modified by an external file.

IV. RESULTS AND DISCUSSION

We desire to know whether we can use graphene to probe the SMMs, in particular their spin states, decorating the surface of graphene by measuring the conductivity of graphene. It

TABLE II. Calculated phonon-limited electron mobility in graphene along the armchair direction as a function of temperature, in 10^4 cm^2 V^{-1} s^{-1}.

Temperature	Mobility
100 K	28.6
200 K	13.3
300 K	3.24

is necessary to know the temperature at which we can expect the carrier mobility to be dominated by the presence of the SMMs on the surface as opposed to the thermal vibrations within graphene. Thus we calculate the phonon limited mobility as well as the SMM limited mobility due to Mn_{12} and $[Mn_3]_2$ on the surface of graphene to compare and make a prediction of the temperature threshold below which we expect to probe the state of the molecule via the carrier mobility. The results on phonon limited mobility in pure graphene are given in Sec. IV A. We present the carrier mobility results for Mn_{12} and $[Mn_3]_2$ in Secs. IV B and IV C, respectively.

A. Phonon limited mobility

The phonon limited carrier mobility is calculated in the armchair direction using the frozen phonon approximation [31] based on a $7 \times 4\sqrt{3}$ orthogonal graphene supercell which consists of 112 C atoms. The repeating $1 \times \sqrt{3}$ unit cell is shown in Figs. 1 and 2. The corresponding screening parameter η for calculating complex bands is found to be 0.680 eV based on Eq. (5). At each temperature (100, 200, and 300 K), 50 different configurations of carbon displacements in the real medium are generated to calculate the carrier mobility [31]. The scattering time τ for each configuration is obtained using Eq. (1). An average scattering time at each temperature is calculated by averaging over all the 50 configurations.

The Fermi level is assumed to be normally distributed with the average Fermi level corresponding to a free electron density of 2×10^{11} cm^{-2} and a standard deviation of 40 meV. The average mobility for each temperature is finally obtained from the ensemble average over different Fermi levels as described above. As shown in Table II, phonon-limited electron mobility in pure graphene increases from 3.24×10^4 cm^2 V^{-1} s^{-1} at 300 K, in good agreement with experimental value of 4×10^4 cm^2 V^{-1} s^{-1} on clean graphene on SiO₂ substrate [32], to 28.6×10^4 cm^2 V^{-1} s^{-1} at 100 K. We will rely on these results to establish the temperature regime in which the carrier mobility in graphene is limited by the adsorption of SMM.

The measurement at 300 K in Ref. [6] without magnetic molecules yielded mobility for both electron and hole carriers that are about one order of magnitude smaller. This is probably because of the presence of unknown defects and scattering from the substrate. Such effects will be modeled in future work.

B. Mn_{12}

The in-plane carrier mobility in graphene is calculated in the presence of a Mn_{12} molecule. Three different mo-

TABLE III. Calculated electron mobility in graphene in the presence of adsorbed Mn_{12} with different ligands, in 10^4 cm^2 V^{-1} s^{-1}.

Ligand	Spin up mobility	Spin down mobility
-H	17.7	17.7
-CH$_3$	35.4	37.1
-CHCl$_2$	3.51	3.52

bilities are computed for different ligands attached to the molecule (-H, -CH$_3$, and -CHCl$_2$). The graphene supercell size is $12 \times 6\sqrt{3}$ of graphene primitive unit cells. This calculation is performed assuming no lattice distortion of due to phonons (effectively $T = 0$ for the lattice) and with electron temperature set at $T = 100$ K. The electron temperature affects both the energy distribution of the electrons as well as the puddling effect. A screening parameter of 0.463 eV obtained from Eq. (5) is used. Both the molecule and the graphene are fully relaxed, and for the complex band calculation, the molecule is omitted and its effect on the graphene is accounted for using the $\delta V = V_{Mn_{12}+Gr} - V_{Gr}$ potential. The δV accounts for the difference in the local potential including both the Hartree potential and the exchange correlation potential. Including the difference in the exchange correlation potential makes δV spin dependent.

We calculate the mobility limited by the molecule for three different ligands of the molecule. The average carrier mobility, shown in Table III, is obtained as an ensemble average over different Fermi-levels as described in Sec. IV A. For the -H and -CH$_3$ ligands, we expect the carrier mobility to be dominated by phonons for temperatures above 200 K, while for the -CHCl$_2$ ligand, we expect the molecule to begin to dominate scattering between 200 and 300 K and its presence on the surface of graphene should have a noticeable impact on the carrier mobility even at room temperature.

The calculated mobility shows large differences between different ligands. Because the mobility for -H and -CH$_3$ is quite higher than phonon-limited mobility at 300 K, one expects that at room temperature these two types of molecules will not show difference in mobility measurements. On the other hand, for -CHCl$_2$ ligand its effect should be noticeable at room temperature. Indeed, this is what was seen experimentally [6] for the hole mobility measurement. Our calculation shows little change in the self-energy as a function of the Fermi energy, therefore we expect electron mobility and hole mobility to be similar. A factor of uncertainty is the concentration of the molecules. Because the calculation and the measurement likely to have quite different concentrations, the absolute values of the mobility are not expected to agree.

C. $[Mn_3]_2$ dimers

We also calculate and compare the in-plane carrier mobility in graphene in the presence of FM and AFM $[Mn_3]_2$ dimers. These dimers differ in their linkers so that the favored magnetic coupling is FM for the FM dimers and AFM for the AFM dimers. The graphene layer contains the same number of carbon atoms as the Mn_{12} calculation. As such, the imaginary screening parameter is also the same as that used in the Mn_{12} mobility calculation. Similar to the case of Mn_{12}, the calcula-

TABLE IV. Calculated electron mobility in graphene in the presence of adsorbed $[Mn_3]_2$ with different orientations, in 10^4 cm^2 V^{-1} s^{-1}.

$[Mn_3]_2$ orientation	Spin up mobility	Spin down mobility
AFM-A	2.15	2.15
AFM-B	1.73	1.73
AFM-C	2.13	2.13
AFM-D	2.01	2.01
Aligned AFM-A	2.15	2.15
Aligned AFM-B	1.73	1.73
Aligned AFM-C	2.13	2.13
Aligned AFM-D	2.01	2.01
FM-A	1.57	1.57
FM-B	2.05	2.05
FM-C	1.83	1.82
FM-D	2.16	2.16

tion is performed in the absence of lattice distortion due to the phonons and with the electron temperature set at $T = 100$ K. In addition to calculating the mobility for different magnetic configurations of the dimer we calculate the mobility for four different orientations A–D [20], as shown in Figs. 5 and 6 for the FM and AFM $[Mn_3]_2$ dimers, respectively. Structural details of these molecules and orientations are given in Ref. [20] The calculated mobilities in graphene under the influence of $[Mn_3]_2$ dimers are summarized in Table IV. For both the AFM and FM $[Mn_3]_2$, their effect on the carrier mobility within graphene should be observable at room temperature for all orientations.

The orientation with the lowest binding energy to graphene do not correspond to the same orientation for the AFM and FM $[Mn_3]_2$ dimers. For AFM configuration, orientation B have the lowest binding energy while for the FM configuration, orientation A has the lowest binding energy [20]. The difference in carrier mobility between AFM-B and FM-A is about 10%. This will be a challenge to experimentally distinguish but not impossible. The orientation AFM-D is only about 0.01 eV above AFM-B [20] but its mobility is another 16% more than that of the AFM-B. Therefore the measured mobility difference between the two types of molecules should be large enough to be seen experimentally when the AFM molecule is averaged between the two orientations.

We also tested the sensitivity of mobility on the magnetic state of the molecules. For this purpose we compared the ground state of the AFM dimer and the states when the moments of the dimer are ferromagnetic aligned (presumably achievable by applying a magnetic field). The very weak spin dependence of δV leads to the result that there is no difference in mobility between these two moment alignments. Therefore mobility is not sensitive to the magnetic states of the molecules when there is no lattice change.

V. CONCLUSION

Using first-principles calculation, we have calculated the carrier mobility in graphene limited by either phonons or the presence of SMMs Mn_{12} and $[Mn_3]_2$ on the surface of
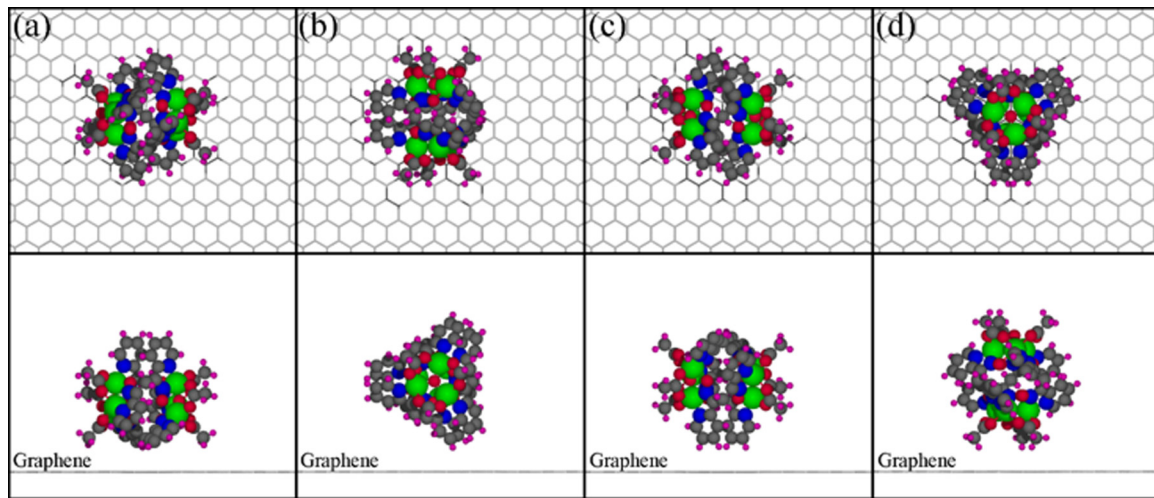
FIG. 5. Orientations of FM [Mn$_3$]$_2$ on graphene. Top (top row) and side (bottom row) views of four adsorption configurations of FM [Mn$_3$]$_2$ dimer on graphene considered in this work. Color code: Mn, green; N, blue; O, red; C in ligand, black; H, pink.

graphene via the complex band structure. We account for most of the scattering effect due to the presence of the molecules on the surface of graphene without having to explicitly include the molecule in the complex band calculation by modifying the local potential, which allows for the possibility of calculating the carrier mobility in graphene limited by the presence of large molecules on the surface.

The large difference in calculated mobility due to Mn$_{12}$ molecules with different ligands is in agreement with experimental measurement [6]. We also predict a significant modest difference in mobility values up to room temperature between AFM and FM [Mn$_3$]$_2$ dimer molecules attached to graphene in their low-energy orientations. These results confirm that mobility measurements can be used to probe and distinguish different magnetic molecules on graphene. Note that these

calculations are performed with the fixed supercell size for different magnetic molecules, implying a fixed molecule concentration. We expect the mobility to scale inversely with the concentration. Therefore reliable differentiation between different molecules in the experiment also requires accurate and independent determination of the concentration.
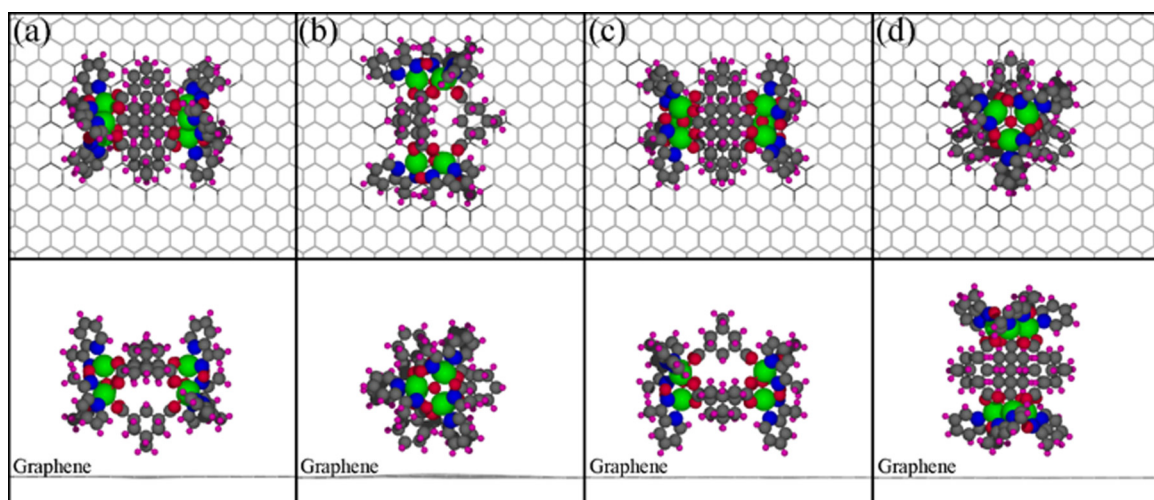
FIG. 6. Orientations of AFM [Mn$_3$]$_2$ on graphene. Top (top row) and side (bottom row) views of four adsorption configurations of AFM [Mn$_3$]$_2$ dimer on graphene considered in this work. Color code: Mn, green; N, blue; O, red; C in ligand, black; H, pink.

[1] W. Han, R. K. Kawakami, M. Gmitra, and J. Fabian, Nat. Nanotechnol. **9**, 794 (2014).

[2] T. O. Wehling, K. S. Novoselov, S. V. Morozov, E. E. Vdovin, M. I. Katsnelson, A. K. Geim, and A. I. Lichtenstein, Nano Lett. **8**, 173 (2008).

[3] A. Candini, S. Klyatskaya, M. Ruben, W. Wernsdorfer, and M. Affronte, Nano Lett. **11**, 2634 (2011).

[4] C. Cervetti, A. Rettori, M. G. Pini, A. Cornia, A. Repollés, F. Luis, M. Dressel, S. Rauschenbach, K. Kern, M. Burghard, and L. Bogani, Nat. Mater. **15**, 164 (2016).

[5] X. Hong, K. Zou, B. Wang, S.-H. Cheng, and J. Zhu, Phys. Rev. Lett. **108**, 226602 (2012).

[6] X. Zhu, A. Hale, G. Christou, and A. F. Hebard, J. Appl. Phys. **127**, 064303 (2020).

[7] X.-G. Li, J. N. Fry, and H.-P. Cheng, Phys. Rev. B **90**, 125447 (2014).

[8] Q. Li, E. H. Hwang, and S. Das Sarma, Phys. Rev. B **84**, 115442 (2011).

[9] C. Joachim, J. K. Gimzewski, and A. Aviram, Nature (London) **408**, 541 (2000).

[10] M. N. Leuenberger and D. Loss, Nature (London) **410**, 789 (2001).

[11] R. Sessoli, H. L. Tsai, A. R. Schake, S. Wang, J. B. Vincent, K. Folting, D. Gatteschi, G. Christou, and D. N. Hendrickson, J. Am. Chem. Soc. **115**, 1804 (1993).

[12] N. E. Chakov, S.-C. Lee, A. G. Harter, P. L. Kuhns, A. P. Reyes, S. O. Hill, N. S. Dalal, W. Wernsdorfer, K. A. Abboud, and G. Christou, J. Am. Chem. Soc. **128**, 6975 (2006).

[13] H.-L. Tsai, H.-A. Shiao, T.-Y. Jwo, C.-I. Yang, C.-S. Wur, and G.-H. Lee, Polyhedron **24**, 2205 (2005).

[14] H. Zhao, C. P. Berlinguette, J. Bacsa, A. V. Prosvirin, J. K. Bera, S. E. Tichy, E. J. Schelter, and K. R. Dunbar, Inorg. Chem. **43**, 1359 (2004).

[15] D. W. Boukhvalov, V. V. Dobrovitski, P. Kögerler, M. Al-Saqer, M. I. Katsnelson, A. I. Lichtenstein, and B. N. Harmon, Inorg. Chem. **49**, 10902 (2010).

[16] T. N. Nguyen, M. Shiddiq, T. Ghosh, K. A. Abboud, S. Hill, and G. Christou, J. Am. Chem. Soc. **137**, 7160 (2015).

[17] J.-X. Yu, G. Christou, and H.-P. Cheng, J. Phys. Chem. C **124**, 14768 (2020).

[18] W. Kohn and L. J. Sham, Phys. Rev. **140**, A1133 (1965).

[19] P. Hohenberg and W. Kohn, Phys. Rev. **136**, B864 (1964).

[20] R. S. Berkley, Z. Hooshmand, T. Jiang, D. Le, A. F. Hebard, and T. S. Rahman, J. Phys. Chem. C **124**, 28186 (2020).

[21] X.-G. Zhang, K. Varga, and S. T. Pantelides, Phys. Rev. B **76**, 035108 (2007).

[22] H. J. Choi and J. Ihm, Phys. Rev. B **59**, 2267 (1999).

[23] A. Smogunov, A. Dal Corso, and E. Tosatti, Phys. Rev. B **70**, 045417 (2004).

[24] G. Kresse, J. Non-Cryst. Solids **193**, 222 (1995).

[25] G. Kresse and D. Joubert, Phys. Rev. B **59**, 1758 (1999).

[26] P. Giannozzi, S. Baroni, N. Bonini, M. Calandra, R. Car, C. Cavazzoni, D. Ceresoli, G. L. Chiarotti, M. Cococcioni, I. Dabo, A. D. Corso, S. de Gironcoli, S. Fabris, G. Fratesi, R. Gebauer, U. Gerstmann, C. Gougoussis, A. Kokalj, M. Lazzeri, L. Martin-Samos *et al.*, J. Phys.: Condens. Matter **21**, 395502 (2009).

[27] P. E. Blöchl, Phys. Rev. B **50**, 17953 (1994).

[28] J. P. Perdew, K. Burke, and M. Ernzerhof, Phys. Rev. Lett. **77**, 3865 (1996).

[29] S. Grimme, J. Antony, S. Ehrlich, and H. Krieg, J. Chem. Phys. **132**, 154104 (2010).

[30] L. Bengtsson, Phys. Rev. B **59**, 12301 (1999).

[31] Y.-N. Wu, X.-G. Zhang, and S. T. Pantelides, Semicond. Sci. Technol. **31**, 115016 (2016).

[32] J.-H. Chen, C. Jang, S. Xiao, M. Ishigami, and M. S. Fuhrer, Nat. Nanotechnol. **3**, 206 (2008).